

# Vertical distribution of aerosols over the Maritime Continent during El Nino

Jason Blake Cohen<sup>1</sup>, Daniel Hui Loong Ng<sup>2</sup>, Alan Wei Lun Lim<sup>3</sup>, Xin Rong Chua<sup>4</sup>

<sup>1</sup>School of Atmospheric Sciences, Sun Yat-Sen University, Guangzhou, China

<sup>2</sup>Tropical Marine Science Institute, National University of Singapore, Singapore

<sup>3</sup>The Chinese University of Hong Kong, Hong Kong, China

<sup>4</sup>Princeton University, Princeton, NJ, USA

*Correspondence to:* Jason Blake Cohen (jasonbc@alum.mit.edu)

## Abstract.

The vertical distribution of aerosols over Southeast Asia, a critical factor impacting aerosol lifetime, radiative forcing, and precipitation, is examined for the 2006 post El-Nino fire burning season. Combining these measurements with remotely sensed land, fire, and meteorological measurements, and fire plume modeling, we have reconfirmed that fire radiative power is underestimated over Southeast Asia by MODIS measurements. These results are derived using a significantly different approach. The horizontally constrained Maritime Continent's fire plume median height, using the maximum variance of satellite observed Aerosol Optical Depth as the spatial and temporal constraint, is found to be  $2.04 \pm 1.52\text{km}$  during the entirety of the 2006 El Nino fire-season, and  $2.19 \pm 1.50\text{km}$  for October 2006. This is  $0.83\text{km}$  ( $0.98\text{km}$ ) higher than random sampling and all other past studies. Additionally, it is determined that  $61(+6-10)\%$  of the bottom of the smoke plume and  $83(+8-11)\%$  of the median of the smoke plume is in the free troposphere during the October maximum; while correspondingly  $49(+7-9)\%$  and  $75(+12-12)\%$  of the total aerosol plume and the median of the aerosol plume, are found in the free troposphere during the entire fire-season. The vastly different vertical distribution will have impacts on aerosol lifetime and dispersal.

Application of a simple plume rise model using measurements of fire properties underestimates the median plume height by  $0.26\text{km}$  over the entire fire season and  $0.34\text{km}$  over the Maximum fire period. It is noted that the model underestimation over the bottom portions of the plume are much larger. The center of the plume can be reproduced when fire radiative power is increased by 20% (with other parts of the plume ranging from an increase of 0% to 60% depending on the portion of the plume and the length of the fire season considered). However, to reduce the biases found, improvements including fire properties under cloudy conditions, representation of small scale convection, and inclusion of aerosol direct and semi-direct effects is required.

## 35 1. Introduction

36 Properly quantifying the vertical distribution of aerosols is essential to constrain their atmospheric  
37 distribution, which in turn impacts the atmospheric energy budget [Ming *et al.*, 2010; Kim *et al.*, 2008],  
38 circulation, clouds and precipitation [Tao *et al.*, 2012; Wang 2013], and human health [Burnett *et al.*, 2014].  
39 However, there are complicating factors including spatial and temporal heterogeneity in emissions [Cohen  
40 and Wang, 2014; Cohen, 2014; Giglio *et al.*, 2006; Petrenko *et al.*, 2012; Wooster *et al.*, 2012], and  
41 uncertainties and non-linearities associated with aerosol processing and removal from the atmosphere [Tao  
42 *et al.*, 2012; Cohen and Prinn, 2011; Cohen *et al.*, 2011]. Furthermore, a lack of sufficiently dense  
43 measurements leads to difficulty constraining the measured distribution of aerosols over scales from  
44 hundreds to thousands of kilometers or over time frames on the decadal to longer time scales [Cohen and  
45 Wang, 2014; Delene and Ogren, 2002; Dubovik *et al.*, 2000; Cohen *et al.*, 2017].

46 Models are very poor at reproducing the actual vertical distribution of atmospheric aerosols  
47 [Cheng *et al.*, 2012; Schuster *et al.*, 2005; Tsigaridis *et al.*, 2014]. They also tend to strongly underestimate  
48 the total atmospheric column loading of aerosols [Colarco *et al.*, 2004; Leung *et al.*, 2007]. Furthermore,  
49 vertical measurements are sparse, and in many regions do not provide adequate statistics to make informed  
50 comparisons with real world conditions. This is no more apparent than over Southeast Asia, where model  
51 studies [Tosca *et al.*, 2011; Martin *et al.*, 2012] have concluded that almost all aerosols are narrowly  
52 confined in the planetary boundary layer, although measurements demonstrate otherwise [Lin *et al.*, 2014].  
53 Presently, there are no known modeling efforts that have been able to reproduce this significant  
54 atmospheric loading and the ensuing vertical distribution.

55 Additionally, aerosol emissions databases in Southeast Asia are quantified using a bottom-up  
56 approach, where small samples and statistics of the activity, land-use, economics, population, and hotspots  
57 are aggregated [van der Werf, 2010; Lamarque, 2010; Bond *et al.*, 2004]. This problem is further  
58 exacerbated by the fact that emissions from organic soils are already not well studied even in non-tropical  
59 regions (Urbanski, 2014). This generally leads to sizable bias: there are few measurements and rapidly  
60 changing land-surface features. A recent couple of papers has used measurements and models in tandem to  
61 quantify a significant underestimation in aerosol emissions over Southeast Asia. This underestimation  
62 occurs both in terms of magnitude [Cohen and Wang, 2014] as well as the spatial and temporal distribution  
63 of the emissions [Cohen, 2014]. In specific, it is significantly impacted on an interannual and intraannual  
64 basis by fires.

65 The vertical distribution is further ill-constrained due to an incomplete understanding of in-situ  
66 production and removal mechanisms which are dependent on washout, which itself is also poorly modeled  
67 [Tao *et al.*, 2012; Wang 2013], especially in the tropics during the dry season [Petersen and Rutledge, 2001;  
68 Ekman *et al.*, 2012]. Heterogeneous aerosol processing may also change the hygroscopicity, which in turn  
69 impacts the washout rate and vertical distribution of the aerosols [Kim *et al.*, 2008; Cohen *et al.*, 2011].  
70 These factors have been shown to combine such that small changes in the initial vertical distribution can  
71 lead to differences in atmospheric transport thousands of kilometers apart [Wang, 2013].

72 The Maritime Continent of Southeast Asia has faced widespread and ubiquitous fires the past few  
73 decades, due to expanding agriculture, urban development, economic growth, and changes in the base  
74 climatology that induce drought [Center, 2005; Dennis et al., 2005; van der Werf et al., 2008; Taylor,  
75 2010]. These fires contribute the major fraction of the atmospheric aerosol burden during the dry season  
76 [Cohen, 2014]. However, these fires are unique: they are relatively low in radiative power and temperature  
77 yet cover a massive net surface area, making their statistics and extent hard to characterize from remote  
78 sensing. Their total emissions are very high, and thus during the burning season they dominate the aerosol  
79 optical depth (AOD) and PM<sub>2.5</sub> levels over thousands of kilometers [Field et al., 2009; Nakajima et al.,  
80 1999]. Due to their widespread and dispersed nature, the fires as a whole in this region are geospatially  
81 coherent in timing and geography, although they may individually burn for different lengths of time, as a  
82 function of localized precipitation and soil moisture, and global circulation patterns such as El-Nino  
83 [Cohen, 2014; Wooster et al., 2012; Hansen, 2008].

84 A comprehensive previous attempt to study aerosol height over Southeast Asia was performed by  
85 Lee et al. [2016]. They used the total The Cloud-Aerosol Lidar with Orthogonal Polarization (CALIOP)  
86 profile, but were not specific about how they cleared or accounted for high ice clouds that frequently found  
87 in this part of the world. They also used day-time data without considering the issues of solar reflection and  
88 backscatter [Winker et al., 2013]. Furthermore, they used satellite derived single scattering albedo (SSA)  
89 approximated by each pass, although this product has been shown to be highly error-prone over Southeast  
90 Asia [Rogers et al., 2009; Hostetler, 2008]. This work did not address how the spatially-disparate individual  
91 path measurements from CALIOP were analyzed or separated in terms of those sampling parts of the fire  
92 plume as compared to those sampling regions not impacted by fires, such as in Cohen [2014] and Cohen et  
93 al. [2017]. Over this region of the world, there has been no direct local validation of the CALIOP product  
94 by other LIDAR related instruments [Sugimoto et al., 2014a]. The only comparisons made so far have been  
95 model-based validation studies [Campbell et al., 2013].

96 This work describes a new approach to comprehensively sample the vertical distribution of smoke  
97 aerosols, by first using decadal scale measurements of AOD from the Multi-angle Imaging  
98 SpectroRadiometer [MISR] satellite [Cohen, 2014], and then separating the smoke impacted regions by  
99 the magnitude of the measured variability. During the 2006 El-Nino enhanced burning, one of the 2 largest  
100 such events over the past 15-year measurement record, this approach yields a much higher vertical aerosol  
101 height than the traditional random sampling approach. A simple plume-rise model [Achtemeier et al., 2011;  
102 Briggs, 1965] using reanalysis meteorology [Kalnay et al., 1996] and measured fire properties was found to  
103 underestimate the measured heights. However, the model could be improved to match the median heights  
104 by increasing the measured fire radiative power [Sessions et al., 2011; Sofiev et al., 2012]. This finding  
105 implies that measured fires may be underestimated in terms of their strength, or that there are missing fires.  
106 However even with scaling, the top and bottom heights of the measured plume still cannot be reproduced.  
107 The data shows that an improved representation of both localized convective transport and the aerosol  
108 direct and semi-direct effects [Ekman et al., 2007; Wang, 2007] are required to make further improvements.

109 It is hoped that these results will provide insight to those working on understanding the strong 2015-2016  
110 El-Nino conditions.

## 111 2. Methods

### 112 2.1 Geography

113 This work is focused on the Maritime Continent, a sub region of Southeast Asia (8°S to 8°N, 95°E  
114 to 125°E) (**Figure 1**) that experiences wide-spread and highly emitting fires on a yearly basis during the  
115 local dry season (starting in August/September and proceeding continuously through October/November).  
116 The combined magnitudes of so many small fires effectively produces a single massive smoke plume in the  
117 atmosphere, that covers much of the region, extending thousands of kilometers [*Cohen*, 2014]. These wide  
118 spread fires are due to anthropogenic clearing of rainforest and agriculture [*Cohen et al.*, 2017; *Dennis et*  
119 *al.*, 2005; *van der Werf et al.*, 2008; *Taylor*, 2010; *Miettinen et al.*, 2013; *Langmann et al.*, 2009]. Over this  
120 region, during the dry season, the removal of aerosols is quite slow, leading to the overall properties of the  
121 plume being relatively consistent over space and time [*Cohen*, 2014]. Therefore, the overall properties of  
122 the smoke plume, when correctly bound in space and time, can be robustly related to the overall properties  
123 of individual fires and daily measurements of AOD from the MISR satellite (**Figure 1**) [*Cohen*, 2014].

124 In 2006, the El-Nino conditions led to an enhanced drought, with subsequent fires lasting from  
125 early September through mid-November. To ensure that this event is uniquely and completely analyzed,  
126 data from September 3<sup>rd</sup> through November 9<sup>th</sup> is ultimately used (more details are given in **Figure 2 and**  
127 **Figure 3a**, which are defined later). The region in (**Figure 1**) consists of the EOF larger than 2.2 (Bjornsson  
128 and Venegas, 1997; *Cohen et al.*, 2017) as calculated from the measured MISR AOD. This region forms the  
129 boundary of the fire source regions (over land) and downwind regions (over both land and sea). This  
130 approach analytically provides a holistic representation in space and time of the impact of individual fires  
131 on the large-scale structure of the aerosol plume. Therefore, the approach allows the vertical distribution of  
132 the smoke to be comprehensively sampled, including those obscured by clouds (very common in this  
133 region), and aged aerosols which were emitted in the fire and transported significantly downwind.

### 134 2.2 Measurements

135 The CALIOP instrument is an active lidar, quantifying the vertically resolved atmospheric  
136 backscatter strength at 532 nm and 1064 nm (a reasonable approximation of the vertical profile of  
137 aerosols), and polarization at 532 nm. The combination of these measurements allows an indication of  
138 particle size (large or small) and whether the particle is a cloud or an aerosol [*Winker et al.*, 2003].  
139 Specifically, we use the backscatter at 532nm and the vertical feature mask (vertical resolution 30m below  
140 8.2km and 60m from 8.2km to 20.2km, horizontal resolution 1/3km) [*Hostetler et al.*, 2006]. To avoid  
141 issues of cloud contamination and solar reflectance only night time data only is used, and any identified  
142 clouds are removed [*Winker et al.*, 2013].

143 Since the width of each pass is narrow, it is not spatially representative in general. However, given  
144 the relative consistency of the plume as a whole, samples constrained within the plume's spatial extent,  
145 taken on the same day, are statistically representative of the smoke plume as a whole [*Cohen*, 2014]. This

146 approach improves upon the approach of Winker et al. [2013] by relaxing the uniform “horizontal box  
147 size”. Instead, the area of analysis is constrained so that in a more general spatial and temporal domain  
148 based on a homogeneous response in measurement space. Specifically, by constraining the region using  
149 AOD, each region therefore has a much larger number of lidar measurements that are consistent with the  
150 physical effects occurring within the region, thereby allowing for improved statistical representation.

151 The extinction-weighted top (10% vertically integrated height), middle-upper (30% vertically  
152 integrated height), median (50% vertically integrated height), middle-lower (70% vertically integrated  
153 height), and bottom (90% vertically integrated height) are computed for each individual measurement, with  
154 the values retained if the aerosol is not in the stratosphere (assumed to be 15km) (**Supplemental Figure 1**).  
155 The data is then aggregated first by day, and second by geography, either into the fire-impacted region, or  
156 the non fire-impacted region, based on (**Figure 1**) [Cohen, 2014]. The aggregated set of measurements is  
157 used to compute probability densities and statistics, demonstrating the vast difference over the fire-  
158 impacted and non-fire impacted regions (**Figures 3a,3b**). The vertical heights both significantly higher and  
159 less variable ( $p<0.01$ ) over the fire region than the non-fire region, inclusively from September 3<sup>rd</sup> through  
160 November 9<sup>th</sup>.

161 Measurements of aerosol optical depth (AOD) [Kaufman et al., 2003], fire radiative power (FRP)  
162 and fire temperature ( $T_F$ ) [Freeborn et al., 2014; Ichoku et al., 2008] are obtained from the MODIS  
163 instrument aboard both the TERRA and AQUA satellites. Version 5, level 2, swath-by-swath measurements,  
164 at daily resolution are used for AOD (best solution 0.55 micron), with a spatial resolution of 10km by 10km,  
165 and FRP/ $T_F$ , with a spatial resolution of 1km by 1km. Given the prevalence of clouds in this region, the  
166 cloud-cleared products are used, leading to a possible low bias in the FRP/ $T_F$  measurements, as well as  
167 some fires not measured at all [Cohen et al., 2017; Freeborn et al., 2014; Ichoku et al., 2008; Kahn et al.,  
168 2008; Kahn et al., 2007]. On the other hand, while some grids are contaminated, the sheer spatial distance  
169 of the plume and the fact that the overwhelming majority of atmospheric aerosols during this time of the  
170 year are due to fires. In fact, there is no observable bias in the overall statistics of the measured AOD  
171 [Cohen, 2014] as observed by looking at the spatially averaged MODIS AOD and statistics over the fire-  
172 constrained and non fire-constrained regions (**Figure 2**). The AOD is higher ( $p<0.01$ ) over the fire-  
173 constrained region, from September 3<sup>rd</sup> through November 9<sup>th</sup>, making the findings consistent with the  
174 approach employing the 12-years worth of MISR measurements, as well as the results from the CALIOP  
175 observations already discussed.

176 In terms of MODIS retrieval uncertainties over land, especially during fire events, there are two  
177 important issues to consider. The first is that under extremely high AOD conditions ( $AOD>2$ ), frequently  
178 aerosols are flagged/reclassified as clouds, which brings about a negative bias. This bias would lead to an  
179 even higher AOD over the fire plume region if it were properly handled, leading to an even larger  
180 difference between “fire region” and the “non-fire region”. The second is the error in the over-land retrieval  
181 can go as high as 15%. However, based on the results in (**Figure 2 and Supplemental Figure 2**), the  
182 difference between the “fire region” and the “non-fire region” is statistically sound even assuming the error

183 is larger than 15%. It is also the reason why MISR was used for the initial definition of the two regions,  
184 since its ability to cloud clear is better than MODIS over this region [Kahn et al., 2010].

185 While there are many errors involved with using the satellite data, the errors in this case are  
186 sufficiently small as to not impact the analysis and results over Southeast Asia during the fire season  
187 (Cohen, 2014; Cohen et al., 2017). The AOD and certain surface products, when used to run models,  
188 have been found to compare in magnitude, spatial, and temporal extent, to various ground based  
189 surface and column measurements, such as from Aerosol Robotic Network [AERONET], the United  
190 States National Oceanic and Atmospheric Administration surface measurement network [NOAA], and  
191 other available air pollution networks. The data-driven models have been shown to lead to a reduction  
192 in the annualized RMS error as compared with the Intergovernmental Panel on Climate Change  
193 Representative Concentration Pathways [IPCC RCP] emissions scenarios by a factor of 2 to 8 against  
194 AERONET stations throughout Asia (Cohen and Wang, 2014). Furthermore, on a month-to-month  
195 basis, the results of the data-driven models have been shown to lead to a reduction in the RMS error  
196 by a factor of 1.8 and of an improvement in the coefficient of determination statistic [ $R^2$ ] by a value of  
197 0.2 to 0.3, when compared against the Global Fire Emissions Database [GFED] dataset (Cohen 2014;  
198 Cohen et al. 2017). Given these findings, it is reasonable to assume that the methodology is as reliable  
199 as anything else presently available.

200

### 201 2.3 Plume Rise Model

202 A simple model is employed to simulate the height to which a parcel of air initially at the surface  
203 over the fire will rise, based on buoyancy, vertical, and horizontal advection (**Supplement**). The  
204 formulation requires information about the temperature and radiative power of the fire as well as local  
205 meteorology [Achtmeier et al., 2011; Briggs, 1965], and yields an idealized height to which aerosols  
206 emitted will rise. The buoyant plume rise is a thermodynamic approximation in nature and thus not as  
207 physically realistic as a large eddy approach, which solves the atmospheric fluid dynamical equations by  
208 parameterizing turbulence at the scale of tens of meters. However, it is less computationally expensive and  
209 more generalizable in the context of approximating the thousands of fires spread geographically over  
210 hundreds of thousands of square kilometers. On the other hand, it is more physically realistic than empirical  
211 relationships from multi-angle measurements [Sofiev et al., 2012], which have also been attempted, but  
212 show poor performance in Southeast Asia.

213 These relationships are efficiently solved using measurements of meteorological and fire  
214 properties, allowing them to be used as rapid parameterizations within regional or global models. However,  
215 there are errors associated with reconciling the different temporal and spatial scales of reanalysis  
216 meteorology, especially convection and associated transport. Secondly, cloud-cover in this region leads to  
217 both missing fires and low-bias in measurements of fire properties [Sofiev et al., 2012; Kaufman et al.,  
218 2003]. Third, the cloud-cover also leads to a heavier contribution of model results in the reanalysis  
219 meteorology. Finally, the effects of the optically thick aerosol plume's feedback on the radiative profile is

220 likely important, but beyond the scope of this work and hence not taken into consideration [Ekman *et al.*,  
221 2007; Wang, 2007].

## 222 3. Results and Discussion

### 223 3.1 Measured Aerosol Vertical Distribution

224 The fire-constrained aggregated daily statistics of the measured vertical aerosol height from  
225 CALIPSO [Winker *et al.*, 2003] is given in (**Figure 3a**), with the aggregated statistics from the October  
226 fire-maximum time and (*the entirety of the fire season*) over the fire-constrained region of the bottom,  
227 middle-lower, median, middle-upper, and top heights respectively:  $1.68 \pm 1.55\text{km}$  ( $1.49 \pm 1.58\text{km}$ ),  
228  $1.92 \pm 1.51\text{km}$  ( $1.76 \pm 1.54\text{km}$ ),  $2.19 \pm 1.50\text{km}$  ( $2.04 \pm 1.52\text{km}$ ),  $2.53 \pm 1.51\text{km}$  ( $2.38 \pm 1.54\text{km}$ ), and  
229  $3.03 \pm 1.52\text{km}$  ( $2.91 \pm 1.57\text{km}$ ) (**Table 1**). These results are supported by the statistical values of aerosol  
230 heights measured by the MPL station in Singapore throughout the period from September 1 to November  
231 30, 2015 (**Supplemental Figure 3**), which are found to range from 1.6km to 2.4km. 2015 was selected to  
232 compare against ground-based lidar measurements, since it was an El-Nino year, and there were no such  
233 measurements available from 2006. It is also known that 2015 in Singapore contained large amounts of  
234 aerosols advected to Singapore from downwind burning sources. Overall, the close resemblance between  
235 these years allows inference from the results.

236 On the other hand, the non fire-constrained region's aggregated statistics of the measured vertical  
237 aerosol height is quite different (**Figure 3b**), with the respective bottom, middle-lower, median, middle-  
238 upper, and top heights during the October maximum-fire period being:  $0.65 \pm 0.98\text{km}$ ,  $0.93 \pm 0.98\text{km}$ ,  
239  $1.21 \pm 1.00\text{km}$ ,  $1.53 \pm 1.02\text{km}$ , and  $1.98 \pm 1.08\text{km}$  (**Table 1**). The average aerosol height over the fire-  
240 constrained region is both much higher and more variable at every vertical level as compared to the non  
241 fire-constrained domain. This difference leads to 61(+6-10)% of the bottom of the smoke plume and 83(+8-  
242 11)% of the median of the smoke plume in the free troposphere during the October maximum; while 49(+7-  
243 9)% and 75(+12-12)% of the respective bottom and median of the aerosol loading is in the free troposphere  
244 over the entirety of the fire-season, over fire-constrained domain. On the other hand, only 17(+10-9)% of  
245 the median of the aerosol loading is located in the free troposphere over the non fire-constrained domain  
246 during the October maximum fire period. However, the variability is roughly constant at all levels over the  
247 fire-constrained region, while the variability increases with vertical level, over the non fire-constrained  
248 region. These results are based on more than 10,000 daily CALIOP measurements.

249 All three findings, higher average aerosol height, larger variance of height, and a consistent  
250 variance of height at all levels, are consistent with areas where most of the aerosol loading is due to surface  
251 fires. Firstly, the buoyancy from fires increases the expected height, with differences in buoyancy from  
252 different strength fires producing random variability in the measured heights. So long as the distribution of  
253 fire strength and meteorology do not differ too much from day-to-day, the variance in aerosol heights  
254 should also not vary much. On the other hand, over non fire-constrained regions, the major contribution to  
255 the vertical aerosol variability is convection, which is expected to increase in variability the higher one  
256 moves upwards from the surface.

257 Furthermore, the relatively constant variability across the heights in the fire-constrained region is  
258 consistent with a proposed radiative-stabilization effect. The extremely high measured AOD values found  
259 by MODIS [Kaufman *et al.*, 2003] over the fire-constrained domain (from 0.5 to 2.0, with most days over  
260 1.0), leads to observable surface cooling (**Figure 2**). Additionally, black carbon aerosols [BC] emitted from  
261 the fire, absorbs incoming solar radiation near the upper portion of the plume, providing a source of  
262 warming. This combination leads to additional stabilization of the atmosphere, and therefore reinforces the  
263 observed vertical aerosol distribution.

264 These results are thus consistent with the observed reduction in in-situ vertical processing over the  
265 regions downwind from the fire sources, but still within the fire-constrained plume region, where buoyancy  
266 from the fires and the self-stabilization effect seem to contribute more than random deep convection.  
267 However, over the non fire-constrained region, given the low AOD and lack of fires, both of these effects  
268 are not observed, and convection dominates, which is consistent with the less uniform vertical distribution.  
269 Given these clear and observed differences, only results from the fire-constrained region will be considered  
270 further.

271 A significant amount of aerosol mass exists in the free troposphere over this region. Assuming the  
272 measured boundary layer height can be represented by the range from 700m to 1300m, with a central value  
273 of 1000m (as observed in Singapore [Chew *et al.*, 2013]) and applied over the domain, the resulting total  
274 loading of aerosols over the boundary layer can be computed. This value, when applied over the entire  
275 geographical domain, the amount of measurements above the boundary layer in October is found to be  
276 [67,61,51]%, [80,70,61]%, [91,83,72]%, [96,92,83]%, and [99,97,94]% respectively of the bottom, lower-  
277 middle, median, upper-middle and top extinction. Although October is slightly more intense, the same  
278 pattern, just to a slightly lesser extent, is found throughout the entire season, with [56,49,40]%,  
279 [72,61,51]%, [87,75,63]%, [96,90,77]%, and [99,97,93]% of the measurements respectively of the bottom,  
280 lower-middle, median, upper-middle and top extinction. This is much higher than previous studies, which  
281 indicated most of the smoke remained within the boundary layer [Tosca *et al.*, 2011].

282 Analysis of the daily measured heights demonstrates 3 statistically unique days: October 11<sup>th</sup>, 15<sup>th</sup>  
283 and 22<sup>nd</sup> (**Table 2**). On the 11<sup>th</sup>, the top and upper-middle measurements fall within the top 15%, while the  
284 median measurements fall within the top 20% of the month's measurements, implying that the result is  
285 consistent with a deep, single layer, extending throughout the lower and middle free-troposphere. The 15<sup>th</sup>  
286 and 22<sup>nd</sup>, while not being as high in the middle-troposphere, also have little to no aerosol in the planetary  
287 boundary layer due to being more confined in the vertical, implying a narrow layer in the middle free-  
288 troposphere. These results are consistent with the measured aerosol layer being mostly in the free  
289 troposphere, a result that is not consistent with the measured FRP or meteorology. This leads to two  
290 important implications. First, that aerosol lifetime on these days will be considerably longer than models  
291 typically reproduce, and thus the radiative forcing will be considerably more warming. Secondly, that the  
292 typical modeling approach which places fresh aerosols directly emitted from the surface, to the given top of



293 the plume, is likely not true. These are two serious issues impacting the ability of most models to be able to  
294 correctly capture the aerosol loading.

295 On the remaining days, the measured heights are consistent on a daily average basis with relatively  
296 uniform emissions, meteorology, and vertical buoyant rise. Although there is some intense but  
297 heterogeneous forcing impacting the vertical distribution, such as localized convection and aerosol cloud  
298 interactions, these are generally not observed to bias the overall plume's properties. Only on October 11<sup>th</sup>,  
299 15<sup>th</sup>, and 22<sup>nd</sup>, are there higher heights or a narrower vertical structure, combined with no readily available  
300 explanation to be found in the fire, AOD, or meteorological properties on these days. This combination can  
301 only be explained by either a clear change in the convection on those days, or some other phenomena not  
302 considered in or otherwise represented by the reanalysis meteorology. The robustness of this approach  
303 assures the validity of these results over the region and time period herein.

304 A comparison between the inverse model by Campbell et al. [2013; Supplemental Figure 6] and  
305 this work's underlying Kalman Filter plus variance maximization modeled fields, shows that this new  
306 modeling approach performs better during the biomass burning season [Cohen, 2014; Cohen and Wang,  
307 2014; Cohen et al., 2017]. Furthermore, the results found using the approach employed here, match well  
308 with individual measurement campaigns lead by Lin Neng-Hui, et al. [2013, 2014, etc.], and the AD-Net  
309 measurement network [Sugimoto et al, 2014b]. The common finding is a small number of on-the-ground  
310 lidar at multiple places within the Northern portion of Southeast Asia and Greater East Asia also observe  
311 something similar. However, since the geographic regions are not identical, therefore they cannot be used to  
312 directly validate the region studied here. But, there is a sufficient amount of similarity, to make an  
313 anecdotal connection. Given these factors, we present the results here as the best available for use at this  
314 time, when targeting this region of the world during the biomass burning season.

### 315 3.2 Measured Fire and Meteorological Properties

316 The daily aggregated measurements of fire radiative power (FRP) [*Freeborn et al.*, 2014; *Ichoku et*  
317 *al.*, 2008] indicate there are 109395 actively burning 1kmx1km pixels in October 2006. However, filtering  
318 for high confidence [Level 9] active fires, reduces this number to 6941 1kmx1km pixels. The respective  
319 measurements have 10%, median, and 90% values of FRP of [115,300,975] W/m<sup>2</sup> for all fires and  
320 [185,540,1495] W/m<sup>2</sup> for high confidence fires (**Table 3**). Overall, these values are much lower than FRP  
321 measured over other intensely burning regions [*Giglio et al.*, 2006]. However, the results are consistent  
322 with the fact that fires in the Maritime Continent occur under relatively wet surface conditions, due to high  
323 levels of mineral-soil moisture, extensive peat, and intermittent localized precipitation [*Couwenberg et al.*,  
324 2010]. These results are based on more than 3000 daily MODIS fire hotspots and associated meteorological  
325 measurements.

326 There is only one day, October 2<sup>nd</sup>, with a statistically high FRP (daily mean more than monthly  
327 90% value), for high confidence fires. Similarly, there are two days, October 28<sup>th</sup> and 30<sup>th</sup>, with an  
328 abnormally low FRP (daily mean less than monthly 15% value), for high confidence fires. None of these  
329 days have a statistically abnormal fire vertical height distribution. However, October 28<sup>th</sup> and 30<sup>th</sup> both

330 show a sizable increase in AOD over the fire constrained region, with the AOD more than 2 standard  
331 deviations greater than the mean over the non fire constrained region, as compared to the period of time  
332 from the 25th through the 27th. One consistent rationale is that there was large-scale precipitation event at  
333 that time, which in turn both increased aerosol removal and wetting of the surface. This in turn led to lower  
334 temperature and FRP and correspondingly higher aerosol emissions factor on these days. Overall, there is  
335 no apparent impact of day-to-day variability of measured FRP driving observed variation in measured  
336 aerosol heights, and hence only high confidence fire data is subsequently used.

337 To examine this hypothesis, the GPCP [Global Precipitation Climatology Project] One-Degree  
338 Daily Precipitation Data Set of global precipitation has been employed to study the amount and duration of  
339 rainfall over the fire-burning and non fire-burning regions [Huffman et al., 2012]. A spatial/temporal  
340 analysis of this dataset, over both the Fire Region and the No-Fire region confirms this hypothesis  
341 (**Supplemental Figure 4**). Overall, there was considerably lower rainfall over the Fire Region than the No-  
342 Fire Region, however, on all days that there was a decrease in AOD and FRP over the Fire Region, there  
343 was a heavy Rainfall at the same time, or one or two days before. The measurements have a correlation  
344 coefficient of -0.39 with a corresponding  $p < 0.01$ . There is no other statistically significant correlation found  
345 over any other combination of the regions with any other combination of rainfall.

346 The Modern-Era Retrospective Analysis for Research and Applications [MERRA] [Rienecker et  
347 al., 2011] reanalysis meteorology is used for the horizontal and vertical wind, and vertical temperature  
348 profile at each location where a fire is measured (**Table 3**). MERRA was chosen because it is based on  
349 NASA satellite measurements, and thus should be more consistent with the measurements used here. With  
350 the exceptions of October 5<sup>th</sup> and 20<sup>th</sup>, the horizontal wind is relatively calm  $6.0 \pm 1.3$  m/s. Also, throughout  
351 the entire month, the vertical temperature gradient is relatively stable  $-5.45 \pm 0.16$  K/km, with only 7  
352 individual fires occurring under unstable atmospheric conditions. Therefore, dynamical instability is not  
353 expected to contribute greatly to the vertical distribution [Stone and Carlson, 1979]. Also, the role played  
354 by the large-scale vertical wind is small  $2.1 \pm 1.6$  mm/s. Given the atmospheric stability and fire-controlled  
355 buoyancy conditions, the plume rise model approach should offer a reasonable approximation of the aerosol  
356 vertical distribution.

357 The approach used here relies upon the atmosphere being either stable or only barely non-stable.  
358 In this part of the world there are two reasons that contribute to most fires occurring under such conditions.  
359 Firstly, that major instability frequently leads to rain, fire suppression, and aerosol wash-out. Secondly that  
360 induced surface cooling and atmospheric heating by the extensive aerosol layer itself tends to increase  
361 atmospheric stability. Such points are made clear in terms of the major unaccounted for processes in the  
362 MERRA data at this resolution: localized convection (due to model resolution), and aerosol cooling and in-  
363 situ heating effects (not incorporated into the underlying model). In theory the direct and semi-direct effect  
364 may be able to be parameterized, but this would require a higher order model. Since these conditions and  
365 effects are not considered by the plume rise model, they therefore cannot be explanations for discrepancies  
366 in the modeled vertical distribution.

### 3.3 Modeled Aerosol Vertical Distribution

Applying the plume rise model, the aggregated daily statistics of the vertical aerosol height at the bottom, lower-middle, median, upper-middle, and top for the October fire-maximum time and (*the entirety of the fire season*) are 0.60km (0.41km), 1.14km (0.88km), 1.85km (1.40km), 2.87km (2.25km), and 4.99km (3.95km) respectively (**Figure 4, Table 4**). The mean of the daily median, lower-middle, and bottom modeled heights are consistently lower than the respective mean of the measured heights for the October fire-maximum time and (*the entirety of the fire season*) by 0.34km (0.64km), 0.78km (0.88km), and 1.08km (1.08km) respectively. The day-to-day differences show that the model generally underestimates the measurements, with the minimum and maximum differences between the two both ranging from -0.92 km to 1.36km, -0.63 km to 2.20km, and -0.19 km to 3.02km, respectively. The upper-middle modeled height is about equal to measurements, with a mean difference for the October fire-maximum time and (*the entirety of the fire season*) of an underestimate of 0.34km over the October maximum to an overestimate of (0.13km) through the entire fire season. The associated day-to-day variations are wide, but are roughly centered around zero, and vary from -1.22km to 1.06km. Finally, the top modeled heights are considerably higher than measurements, with an average overestimate for the October fire-maximum time and (*the entirety of the fire season*) being 1.96km and (1.04km) respectively. The day-to-day difference between the model and the measurements generally overestimates the measurements, with a value varying from -1.54 to 0.81km.

The model underestimates the height of the median through bottom of the plume, while simultaneously overestimating the top. First, this means that the model is not accounting for enough energy to obtain the average rise of the plume. At the same time, the modeled vertical spread is too large, implying other factors limit the height gain near the top of the plume and enhance the height near the bottom. The results are consistent with one or both of the two hypothesized effects; first, that a low bias exists in the measured values of FRP [*Kahn et al., 2007; Kahn et al., 2008*], leading to insufficient buoyancy. Second, that in-situ stabilization occurs due to aerosol radiative cooling in the lower parts of the plume and aerosol radiative heating within the upper parts of the plume. This combination of factors is also consistent with the observed underestimate in measured FRP to match the median height, as well as the hypothesized complete non-detection of small fires [*Kaufman et al., 2003*]. There are also uncertainties in the MERRA reanalysis products, but given the large sample size and the narrowness of the MERRA distribution, the impact of these uncertainties is around 10%, which as we show later is considerably smaller than changes in the FRP.

A sensitivity analysis is used to quantify the effects of a low bias in FRP, by applying a constant multiplicative factor to the measured FRP for each fire, from 1.0 to 2.0 in steps of 0.1 (although only the results in steps of 0.2 are given in **Table 4**). Although there are also uncertainties associated with measured vertical wind and temperature structure, this is not considered (**Table 3**), since there is no way to couple meteorological effects at sub-grid scale, or otherwise not included in the reanalysis meteorology. The results are obtained by minimizing the root-mean square (RMS) difference between the daily measured and modeled heights, for each FRP scaling factor, at each of the middle-upper, median, and middle-lower levels. The respective best-fit enhancement factors over the October fire maximum (and the entire fire

405 season) are **1.0 (1.0)** for middle-upper measurements, having an RMS error of 0.69km (0.66km); **1.2 (1.2)**  
406 for median measurements, having an RMS error of 0.78km (0.72km); and **1.6 (1.4)** for middle-lower  
407 measurements, having an RMS error of 0.92km (0.82km) (**Figure 4**).

408 Another source of uncertainty is due to the height of the boundary layer itself, which is also  
409 uncertain, due to both a lack of measurements, and a poor ability of reanalysis and other global scale  
410 products to simulate the boundary layer in this part of the world. As before, the model was run in a  
411 sensitivity mode, assuming 3 different average boundary layer heights. The results for the middle-upper,  
412 median, and middle-lower levels best fit values over the October fire maximum (and the entirety of the fire  
413 season) are enhancements of 1.0, 1.4, and 1.8 and (1.0, 1.1, and 1.5) respectively for a boundary layer  
414 height of 1300m and 1.0, 1.3, and 1.6 and (1.0, 1.1, and 1.4) for a boundary layer height of 700m. These  
415 results show that this factor is highly important in terms of modulating the magnitude of the best-fitting  
416 FRP scaling factor. However, a similar biases still exists, where the model is reasonably good at  
417 reproducing the upper-middle levels of the plume, but is incapable of reproducing the median and middle-  
418 lower levels of the plume. Additionally, the larger values of the RMS error at the two more extreme  
419 boundary layer heights lend further support to the initial supposition: overall the boundary layer height  
420 throughout the fire region, lies within these boundaries.

421 Although there is no single best-fit FRP scaling factor, a reasonable fit of the model, based on  
422 measured values from the middle-lower to the middle-upper plume levels can be obtained by using an  
423 appropriate FRP enhancement. The results establish that current plume rise models can reproduce the  
424 median vertical plume height over Southeast Asia by increasing the FRP by 20%, a finding consistent with  
425 FRP generally underestimated over this region. By changing the FRP enhancement from 0% to 60%, the  
426 central 40% of the aerosol plume's vertical extent can be modeled, although the top and bottom heights of  
427 the plume cannot be reproduced. Additionally, the modeled plume is widely spread as compared to the  
428 narrowness of the measured plume. Unfortunately, rectifying these limitations will likely require the use of  
429 a more complex modeling approach and improvement of measured fire data.

430 There are additional errors associated with the non-complete complexity of the models employed.  
431 The models do not capture the contribution of atmospheric stabilization due to both the direct and semi-  
432 direct aerosol effects. Furthermore, these models do not take into account the impacts of localized  
433 convection. However, the majority of other works that employ regional and global models use this exact  
434 same methodology, and hence they also neglect these same small-scale phenomena in terms of  
435 communication between the chemistry, radiation, and the meteorology.

## 436 4. Conclusions

437 This work quantifies the significant present-day underestimation of the vertical distribution of  
438 aerosols over the Maritime Continent during an El-Nino influenced fire season, by introducing a new  
439 method to appropriately constrain the measurements over the geographical region of the aerosol plume.  
440 While this was a large-scale fire event, it was very special, because it occurred throughout almost all of  
441 September, and all the way through the first third of November. Typically the wet-season arrives in this part

442 of the world sometime by the middle of October. And because of this, the wetness of the soil and the large-  
443 scale meteorological flow, were both different this year from a more typical year. As a result, the measured  
444 heights over the constrained region are found to be higher than previously thought. This year about 61(+6-  
445 10)% of the bottom of the aerosol layer and 83(+8-11)% of the median of the aerosol layer being in the free  
446 troposphere during the October maximum; while correspondingly 49(+7-9)% and 75(+12-12)% of the total  
447 aerosol height and the median of the aerosol plume are found in the free troposphere during the entirety of  
448 the fire-season. Due to the considerably higher vertical rise, the aerosols can be advected thousands of  
449 kilometers from their sources and have a greater impact on the atmospheric and climatic systems.

450 Additionally, over the fire-constrained region, the vertical variability of the plume is found to be uniform  
451 throughout its height, implying that it is controlled mostly by local forcing, such as the buoyancy released  
452 by fires, localized convection, and aerosol/radiative feedbacks, such as the direct and semi-direct effects.

453 Application of a plume-rise model showed that there was an overall low bias against measured  
454 heights. This is consistent with the FRP being underestimated in this region of the world due to large-scale  
455 cloud cover. It was also determined that measured vertical heights are more narrowly confined in the  
456 vertical than those simulated by models. A robust sensitivity analysis found that the middle-lower through  
457 middle-upper extent of the plume can be reproduced if an appropriate (although changing) enhancement is  
458 applied to the FRP ranging from 1.0\*FRP to 1.6\*FRP over the maximum period of the fire season, through  
459 the month of October (and from 1.0\*FRP to 1.4\*FRP over the fire season as a whole, for most of  
460 September, all of October, and the first third of November). Hence, the variable FRP enhancement factor  
461 approach can allow for improved modeling of the height statistics for the middle-upper to middle-lower  
462 extent of the plume.

463 However, it is not possible to reproduce either the top or bottom of the measured heights, the  
464 knowledge of which is important to constrain the impacts of long-range transport and aerosol-climate  
465 interactions. Nor is it possible to reproduce the narrow spread of the measured heights. The results are  
466 consistent with the general understanding of current model shortcomings. Hence both the underestimation  
467 of FRP values and current shortcomings in models need to be addressed, if we are to successfully model the  
468 vertical aerosol distribution over this region of the world.

469 The results have been found to be robust over a region that behaves roughly uniformly over  
470 thousands of kilometers, including regions both near and far from the source of the fires. Since there are  
471 only a few days that have relatively unique aerosol and meteorological properties over the period studied,  
472 the results support a few robust conclusions. First, if we want to improve the ability to model aerosol  
473 heights, newer modelling approaches and improvements that will be able to resolve local-scale forcing,  
474 such as deep convection, aerosol/radiation interactions, and aerosol-cloud interactions need to be  
475 considered. Second, the biased underestimation of FRP is also an important point to improve the aerosol  
476 height modeling, especially under conditions where cloudiness occurs or the measured AOD levels are very  
477 high. These errors are exacerbated over regions where large-scale precipitation is very low or where there is  
478 substantial aerosol/cloud intermixing. In all cases, until these model and measurement improvements are

479 made, there is expected to be a significant underestimation of the aerosol loadings and radiative forcing  
480 distribution regionally, and to some extent globally. It is hoped that in the interim, the community will adapt  
481 a variable enhancement of FRP in tandem with measurement-constrained boundaries of smoke plumes, as a  
482 way to more precisely reproduce the statistics of the vertical aerosol distribution.

483 **Acknowledgements:**

484 We would like to acknowledge the PIs of the NASA MODIS, MISR, and CALIPSO projects for providing  
485 the data. The work was supported by the Chinese National Young Thousand Talents Program (Project  
486 74110-41180002), the Chinese National Natural Science Foundation (Project 74110-41030028), and the  
487 Guangdong Provincial Young Talent Support Fund (Project 74110-42150003).

488 **References:**

- 489 Achtemeier, G., S. Goodrick, Y. Liu, F. Garcia-Menendez, Y. Hu, and M. Odman, (2011). Modeling smoke  
490 plume-rise and dispersion from Southern United States prescribed burns with daysmoke.  
491 *Atmosphere*, 2, 358-388.
- 492 Bjornsson, H. and Venegas, S. (1997). A Manual for EOF and SVD Analyses of Climate Data. Department  
493 of Atmospheric and Oceanic Sciences and Centre for Climate and Global Change Research, Tech.  
494 rep., McGill University, Technical Report, 1997.
- 495 Bond, T. C., D.G. Streets, K.F. Yarber, S.M. Nelson, J.H. Woo, and Z. Klimont. (2004). A technology-based  
496 global inventory of black and organic carbon emissions from combustion, *J. Geophys. Res.*, 109,  
497 D14203, doi:10.1029/2003JD003697.
- 498 Briggs, G. A. (1965). A plume rise model compared with observations. *Journal of the Air Pollution Control*  
499 *Association*, vol. 15, no. 9, pp. 433–438.
- 500 Burnett, R., A. Pope, M. Ezzati, C. Olives, S. Lim, S. Mehta, H. Shin, G. Singh, B. Hubbell, M. Brauer, R.  
501 Anderson, K. Smith, J. Balmes, N. Bruce, H. Kan, F. Laden, A. Pruss-Ustun, M. Turner, S. Gapstur,  
502 R. Diver, and A. Cohen. (2014) An Integrated Risk Function for Estimating the Global Burden of  
503 Disease Attributable to Ambient Fine Particulate Matter Exposure, *Environ Health Perspect*;  
504 doi:10.1289/ehp.1307049.
- 505 Campbell, J.R., Reid, J.S., Westphal, D.L., Zhang, J.L., Tackett, J.L., Chew, B.N., Welton, E.J., Shimizu,  
506 A., Sugimoto, N., Aoki, K., Winker, D.M. (2013) Characterizing the vertical profile of aerosol  
507 particle extinction and linear depolarization over Southeast Asia and the Maritime Continent: The  
508 2007–2009 view from CALIOP, *Atmospheric Research*, 122, March 2013, 520–543,  
509 <http://dx.doi.org/10.1016/j.atmosres.2012.05.007>.
- 510 Chew, B. N., J.R. Campbell, S.V. Salinas, C.W. Chang, J.S. Reid, E.J. Welton, and S.C. Liew. (2013).  
511 Aerosol particle vertical distributions and optical properties over Singapore. *Atmospheric*  
512 *Environment*, 79, 599-613.
- 513 Chung, C. E., V. Ramanathan and D. Decremer. (2012) Observationally constrained estimates of  
514 carbonaceous aerosol radiative forcing, *Proc. Natl. Acad. Sci. U.S.A.*,  
515 doi:10.1073/pnas.1203707109.
- 516 Cohen, J. B. and Prinn, R. G. (2011). Development of a fast, urban chemistry metamodel for inclusion in  
517 global models, *Atmos. Chem. Phys.*, 11, 7629–7656, doi:10.5194/acp-11-7629-2011.
- 518 Cohen, J. B. (2014) Quantifying the occurrence and magnitude of the Southeast Asian fire climatology.  
519 *Environmental Research Letters*, 9(11), 114018.
- 520 Cohen, J. B., Lecoœur, E., and Hui Loong Ng, D. (2017) Decadal-scale relationship between measurements  
521 of aerosols, land-use change, and fire over Southeast Asia, *Atmos. Chem. Phys.*, 17, 721-743,  
522 doi:10.5194/acp-17-721-2017.
- 523 Cohen, J. B. and Wang C (2014) Estimating Global Black Carbon Emissions Using a Top-Down Kalman  
524 Filter Approach. *J. Geophys. Res.*, doi:10.1002/2013JD019912.



525 Colarco, P., M. Schoeberl, B. Doddridge, L. Marufu, O. Torres, and E. Welton. (2004) Transport of smoke  
526 from Canadian forest fires to the surface near Washington, D.C.: Injection height, entrainment, and  
527 optical properties, *J. Geophys. Res.*, 109, D06203, doi:10.1029/2003jd00424.

528 Couwenberg, J., R. Dommain, and H. Joosten, H. (2010). Greenhouse gas fluxes from tropical peatlands in  
529 south-east Asia. *Global Change Biology*, 16: 1715–1732. doi:10.1111/j.1365-2486.2009.02016.

530 Delene, D. J. and J.A. Ogren (2002) Variability of aerosol optical properties at four North American  
531 surface monitoring sites, *J. Atmos. Sci.*, 59(6), 1135–1150.

532 Dennis, R. A., J. Mayer, G. Applegate, U. Chokkalingam, C.J.P. Colfer, I. Kurniawan, and T.P. Tomich.  
533 (2005). Fire, people and pixels: linking social science and remote sensing to understand underlying  
534 causes and impacts of fires in Indonesia. *Human Ecology*, 33(4), 465-504.

535 Dubovik, O., A. Smirnov, B.N. Holben, M.D. King, Y.J. Kaufman, T.F. Eck and I Slutsker. (2000)  
536 Accuracy assessments of aerosol optical properties retrieved from Aerosol Robotic Network  
537 (AERONET) Sun and sky radiance measurements. *J. Geophys. Res.*, 105(D8), 9791-9806.

538 Ekman, A., A. Engstrom and C. Wang. (2007). The effect of aerosol composition and concentration on the  
539 development and anvil properties of a continental deep convective cloud, *Q. J. Roy. Meteor. Soc.*,  
540 133B(627), 1439-1452.

541 Ekman, A. M. L., M. Hermann, P. Gross, J. Heintzenberg, D. Kim, and C. Wang. (2012). Sub-micrometer  
542 aerosol particles in the upper troposphere/lowermost stratosphere as measured by CARIBIC and  
543 modeled using the MIT-CAM3 global climate model, *J. Geophys. Res.*, 117, D11202,  
544 doi:10.1029/2011JD016777.

545 Field, R. D., G.R. van der Werf, S.P.P. Shen. (2009) Human amplification of drought-induced biomass  
546 burning in Indonesia since 1960. *Nature Geosci.*, 10.1038/ngeo443.

547 Freeborn, P. H., M.J. Wooster, D.P. Roy and M.A. Cochrane. (2014). Quantification of MODIS fire  
548 radiative power (FRP) measurement uncertainty for use in satellite-based active fire characterization  
549 and biomass burning estimation, *Geophys. Res. Lett.*, 41, 1988–1994, doi:10.1002/2013GL59086.

550 Giglio, L., I. Csiszar and C.O. Justice. (2006) Global distribution and seasonality of active fires as observed  
551 with the Terra and Aqua MODIS sensors. *J. Geophys. Res.*, doi:10.1029/2005JG000142.

552 Hansen, M. C. (2008). Humid tropical forest clearing from 2000 to 2005 quantified by using multitemporal  
553 and multiresolution remotely sensed data. *Proc. Natl. Acad. Sci. USA*, 105, 9439–9444.

554 Hostetler, C., Hair, J., Liu, Z.Y., Ferrare, R., Harper, D., Cook, A., Vaughan, M., Trepte, C., Winker, D.  
555 (2008) Validation of CALIPSO Lidar Observations Using Data From the NASA Langley Airborne  
556 High Spectral Resolution Lidar (Retrieved from:  
557 <https://ntrs.nasa.gov/archive/nasa/casi.ntrs.nasa.gov/20080014234.pdf>)

558 Hostetler, C, Z. Liu, J. Reagan, M. Vaughan, D. Winker, M. Osborn, W. Hunt, K. Powell, and C. Trepte.  
559 (2006). CALIOP Algorithm Theoretical Basis Document–Part 1: Calibration and Level 1 Data  
560 Products. *Doc. PC-SCI 201*.

561 Huffman, G.J., Bolvin, D.T., and Adler, R.F. (2012) last updated 2012: GPCP Version 1.2 1-Degree Daily  
562 (1DD) Precipitation Data Set. WDC-A, NCDC, Asheville, NC. Data set accessed November 1, 2017  
563 at <http://www.ncdc.noaa.gov/oa/wmo/wdcametncdc.html>.

564 Ichoku, C., L. Giglio, M. Wooster and L. Remer. (2008). Global characterization of biomass-burning  
565 patterns using satellite measurements of fire radiative energy. *Remote Sensing of Environment* 112.6,  
566 2950-2962.

567 Kahn, R.A., Gaitley B.J., Garay M.J., Diner, D.J., Eck, T.F., Smirnov, A., and Holben, B.N. (2010)  
568 Multiangle Imaging SpectroRadiometer global aerosol product assessment by comparison with the  
569 Aerosol Robotic Network. *J. Geophys. Res. Atmos.* 115, D23209, doi:10.1029/2010JD014601

570 Kahn, R.A., Chen, Y., Nelson, D.L., Leung, F.Y., Li, Q.B., Diner, D.J., and Logan, J.A. (2008). Wildfire  
571 smoke injection heights: Two perspectives from space. *Geophys. Res. Lett.*, 35, L04809,  
572 doi:10.1029/2007GL032165.

573 Kahn, R.A., Li, W.H., Moroney, C., Diner, D.J., Martonchik, J.V., and Fishbein, E. (2007). Aerosol source  
574 plume physical characteristics from space-based multiangle imaging. *J. Geophys. Res.*, 112,  
575 D11205, doi:10.1029/2006JD007647, 2007

576 Kalnay et al. (1996). The NCEP/NCAR 40-year reanalysis project, *Bull. Amer. Meteor. Soc.*, 77, 437-470.

577 Kaufman, Y. J., C. Ichoku, L. Giglio, S. Korontzi, D.A. Chu, W.M. Hao, and C.O. Justice. (2003). Fire and  
578 smoke observed from the Earth Observing System MODIS instrument--products, validation, and  
579 operational use. *International Journal of Remote Sensing*, 24(8), 1765-1781.

580 Kim, D., C. Wang, A.M.L. Ekman, M. C. Barth, and P. Rasch. (2008) Distribution and direct radiative  
581 forcing of carbonaceous and sulfate aerosols in an interactive size-resolving aerosol-climate model,  
582 *J. Geophys. Res.*, 113, D16309, doi:10.1029/2007JD009756.

583 Lamarque, J. F. (2010). Historical (1850–2000) gridded anthropogenic and biomass burning emissions of  
584 reactive gases and aerosols: methodology and application. *Atmos. Chem. Phys.*, doi:10.5194/acp-10-  
585 7017-2010.

586 Langmann, B., B. Duncan, C. Textor, J. Trentmann, and G.R. van der Werf. (2009). Vegetation fire  
587 emissions and their impact on air pollution and climate. *Atmospheric Environment*, 43(1), 107-116.

588 Lee, J., Hsu, N.C., Bettenhausen, C., Sayer, A.M., Seftor, C.J., Jeong, M.J., Tsay, S.C., Welton, E.J., Wang,  
589 S.H., Chen, W.N. (2016) Evaluating the Height of Biomass Burning Smoke Aerosols Retrieved  
590 from Synergistic Use of Multiple Satellite Sensors over Southeast Asia, *Aerosol and Air Quality*  
591 *Research*, 16: 2831–2842 doi:10.4209/aaqr.2015.08.0506

592 Leung, F.Y.T., J.A. Logan, R. Park, E. Hyer, E. Kasischke, D. Streets, and L. Yurganov. (2007) Impacts of  
593 enhanced biomass burning in the boreal forests in 1998 on tropospheric chemistry and the sensitivity  
594 of model results to the injection height to emissions. *J. Geophys. Res.*, 112, D10313,  
595 doi:10.1029/2006JD008132.

596 Lin, N. H., A.M. Sayer, S.H. Wang, A.M. Loftus, T.C. Hsiao, G.R. Sheu, and S. Chantara. (2014).  
597 Interactions between biomass-burning aerosols and clouds over Southeast Asia: Current status,  
598 challenges, and perspectives. *Environmental Pollution*, 195, 292-307.

599 Martin, V.M., R.A. Kahn, J.A. Logan, R. Paugam, M. Wooster, and C. Ichoku. (2012). Space-based  
600 observational constraints for 1-D fire smoke plume-rise models. *Journal of Geophysical Research:*  
601 *Atmospheres (1984–2012)*, 117(D22).

602 Miettinen, J., E. Hyer, A.S. Chia, L.K. Kwok, and S.C. Liew, S. C. (2013). Detection of vegetation fires  
603 and burnt areas by remote sensing in insular Southeast Asian conditions: current status of knowledge  
604 and future challenges. *International journal of remote sensing*, 34(12), 4344-4366.

605 Ming, Y., V. Ramaswamy and G. Persad. (2010) Two opposing effects of absorbing aerosols on global-  
606 mean precipitation. *Geophysical Research Letters* 37.13.

607 Nakajima, T., A. Higurashi, N. Takeuchi and J.R. Herman (1999). Satellite and ground-based study of  
608 optical properties of 1997 Indonesian Forest Fire aerosols. *Geophys. Res. Lett.*,  
609 10.1029/1999GL900208.

610 Petersen, W. and S. Rutledge. (2001). Regional Variability in Tropical Convection: Observations from  
611 TRMM. *J. Climate*, 14, 3566–3586.

612 Petrenko, M., R.A. Kahn, M. Chin, A.J. Soja, T. Kucsera, and Harshvardhan. (2012) The use of satellite-  
613 measured aerosol optical depth to constrain biomass burning emissions source strength in the global  
614 model GOCART, *J. Geophys. Res.*, doi:10.1029/2012JD01787.

615 Rienecker, M.M., M.J. Suarez, R. Gelaro, R. Todling, J. Bacmeister, E. Liu, M.G. Bosilovich, S.D.  
616 Schubert, L. Takacs, G.-K. Kim, S. Bloom, J. Chen, D. Collins, A. Conaty, and A. da Silva (2011).  
617 MERRA: NASA's Modern-Era Retrospective Analysis for Research and Applications. *J. Climate*,  
618 24, 3624-3648, doi:10.1175/JCLI-D-11-00015.1

619 Rogers, R.R., Hostetler, C.A., Ferrare, R.A., Hair, J.W., Obland, M.D., Cook, A.L., Harper, D.B., Swanson,  
620 A.J. (2009) Validation of CALIOP Aerosol Backscatter and Extinction Profile Products Using  
621 Airborne High Spectral Resolution Lidar Data (Retrieved from:  
622 [http://cimss.ssec.wisc.edu/calipso/meetings/cloudsat\\_calipso\\_2009/Posters/Rogers.pdf](http://cimss.ssec.wisc.edu/calipso/meetings/cloudsat_calipso_2009/Posters/Rogers.pdf))

623 Schuster, G. L., O. Dubovik, B. Holben and E. Clothiaux. (2005) Inferring black carbon content and  
624 specific absorption from Aerosol Robotic Network (AERONET) aerosol retrievals, *J. Geophys.*  
625 *Res.*, 110, D10S17, doi:10.1029/2004JD004548.

626 Sessions, W. R., H.E. Fuelberg, R.A. Kahn, and D.M. Winker. (2011). An investigation of methods for  
627 injecting emissions from boreal wildfires using WRF-Chem during ARCTAS. *Atmospheric*  
628 *Chemistry and Physics*, 11(12), 5719-5744.

629 Sofiev, M., T. Ermakova, and R. Vankevich. (2012). Evaluation of the smoke-injection height from  
630 wildland fires using remote-sensing data. *Atmos. Chem. Phys*, vol. 12, no. 4, pp. 1995–2006.

631 Stone, P. and J. Carlson. (1979). Atmospheric Lapse Rate Regimes and Their Parameterization. *J. Atmos.*  
632 *Sci.*, 36, 415–423.

633 Sugimoto, N., Nishizawa T., Shimizu A., Matsui I., Jin Y. (2014a) Characterization of aerosols in East Asia  
634 with the Asian dust and aerosol lidar observation network (AD-Net) *Proc. SPIE* 9262 92620K  
635 Sugimoto, N., Shimizu, A., Nishizawa, T., Matsui, I., Jin, Y., Khatri, P., Irie, H., Takamura, T., Aoki, K.,  
636 Thana, B. (2014b) Aerosol characteristics in Phimai, Thailand determined by continuous  
637 observation with a polarization sensitive Mie–Raman lidar and a sky radiometer, *Environmental*  
638 *Research Letters*, 10, 6.

639 Tao, W.K., J.P. Chen, Z.Q. Li, C. Wang, and C.D. Zhang. (2012) The Impact of Aerosol on convective  
640 cloud and precipitation. *Rev. Geophys.*, 50, RG2001, doi:10.1029/2011RG000369.

641 Taylor, D. (2010). Biomass burning, humans and climate change in Southeast Asia. *Biodiversity and*  
642 *conservation*, 19(4), 1025-1042.

643 Tosca, M. G., J.T. Randerson, C.S. Zender, D.L. Nelson, D.J. Diner, and J.A. Logan (2011), Dynamics of  
644 fire plumes and smoke clouds associated with peat and deforestation fires in Indonesia, *J. Geophys.*  
645 *Res.*, 116, D08207, doi:10.1029/2010JD015148.

646 Tsigaridis, K., N. Daskalakis, M. Kanakidou, P.J. Adams, P. Artaxo, R. Bahadur, Y. Balkanski, S.E.  
647 Bauer, N. Bellouin, A. Benedetti, T. Bergman, T.K. Berntsen, J.P. Beukes, H. Bian, K.S.  
648 Carslaw, K. S., M. Chin, G. Curci, T. Diehl, R.C. Easter, S.J. Ghan, S.L., Gong, A. Hodzic, C.R.  
649 Hoyle, T. Iversen, S. Jathar, J.L. Jimenez, J.W. Kaiser, A. Kirkevag, D. Koch, H. Kokkola, Y.H.  
650 Lee, G. Lin, X. Liu, C. Luo, X. Ma, G.W. Mann, N. Mihalopoulos, J.J. Morcrette, J.F. Müller, G.  
651 Myhre, S. Myriokefalitakis, N.L. Ng, D. O'Donnell, J.E. Penner, L. Pozzoli, K.J. Pringle, L.M.  
652 Russell, M. Schulz, J. Sciare, O. Seland, D.T. Shindell, S. Sillman, R.B. Skeie, D. Spracklen, T.  
653 Stavroukou, S.D. Steenrod, T. Takemura, P. Tiitta, S. Tilmes, H. Tost, T. van Noije, P.G. van Zyl, K.  
654 von Salzen, F. Yu, Z. Wang, Z. Wang, R.A. Zaveri, H. Zhang, K. Zhang, Q. Zhang, and X.  
655 Zhang, X. (2014) The AeroCom evaluation and intercomparison of organic aerosol in global  
656 models, *Atmos. Chem. Phys.*, 14, 10845-10895, doi:10.5194/acp-14-10845-2014.

657 Urbanski. Shawn (2014) Wildland fire emissions, carbon, and climate: Emission factors, *Forest Ecology*  
658 *and Management*, 317, 51–60.

659 van der Werf, G. R. (2010). Global fire emissions and the contribution of deforestation, savanna, forest,  
660 agricultural, and peat fires (1997–2009). *Atmos. Chem. Phys.*, 10.5194/acp-10-11707-2010.

661 van der Werf, G. R., J. Dempewolf, S.N. Trigg, J.T. Randerson, P.S. Kasibhatla, L. Giglio, and R.S. DeFries.  
662 (2008). Climate regulation of fire emissions and deforestation in equatorial Asia. *Proceedings of the*  
663 *National Academy of Sciences*, 105(51), 20350-20355.

664 Wang, C. (2013) Impact of anthropogenic absorbing aerosols on clouds and precipitation: A review of  
665 recent progresses, *Atmos. Res.*, 122, 237-249.

666 Wang, C. (2007). Impact of direct radiative forcing of black carbon aerosols on tropical convective  
667 precipitation, *Geophys. Res. Lett.*, 34, L05709, doi:10.1029/2006GL028416.

668 Winker, D. M., J. Pelon, and M.P. McCormick (2003), The CALIPSO mission: Spaceborne lidar for  
669 observation of aerosols and clouds, *Proc. SPIE*, 4893, 1–11.

- 670 Winker, D. M., Tackett, J. L., Getzewich, B. J., Liu, Z., Vaughan, M. A., and Rogers, R. R.: The global 3-D  
671 distribution of tropospheric aerosols as characterized by CALIOP, *Atmos. Chem. Phys.*, 13, 3345-  
672 3361, <https://doi.org/10.5194/acp-13-3345-2013>, 2013.
- 673 Woodward J. L. (2010). *Estimating the Flammable Mass of a Vapour Cloud: A CCPS Concept Book*, John  
674 Wiley & Sons, ISBN 0470935359, 9780470935354.
- 675 Wooster, M. J., G.L.W. Perry and A. Zoumas. (2012) Fire, drought and El Niño relationships on Borneo  
676 (Southeast Asia) in the pre-MODIS era (1980–2000), *Biogeosciences*, 9, 317-340, doi:10.5194/bg-9-  
677 317-2012.

678  
679  
680  
681  
682  
683  
684  
685

**Table 1:** Statistical summary of measured CALIPSO smoke plume heights in the El-Nino Season of 2006, at different percentiles of extinction height (top/Z=10%, middle-upper/ Z=30%, median/Z=50%, middle-lower/Z=70%, and bottom/Z=90%). The numbers in normal print correspond to the data during the **maximum of the fire season in October**, while those numbers in *(italics)* correspond to the **entire fire season from September 3<sup>rd</sup> through November 9<sup>th</sup>**. All data is further divided into the subset of the Maritime Continent **impacted by smoke (FIRE)**, and **not impacted by smoke (NO-FIRE) (Figure 1)**. “MEAN” is the average, “STD” is the standard deviation, and percentages XX% are the corresponding distribution’s percentiles.

	bottom [km]	middle-lower [km]	median [km]	middle-upper [km]	top [km]
<b>FIRE 5%</b>	0.18 ( <i>0.17</i> )	0.35 ( <i>0.35</i> )	0.56 ( <i>0.57</i> )	0.85 ( <i>0.77</i> )	1.27 ( <i>1.14</i> )
<b>FIRE 10%</b>	0.25 ( <i>0.22</i> )	0.48 ( <i>0.46</i> )	0.74 ( <i>0.68</i> )	1.06 ( <i>1.02</i> )	1.50 ( <i>1.47</i> )
<b>FIRE 15%</b>	0.30 ( <i>0.26</i> )	0.58 ( <i>0.52</i> )	0.88 ( <i>0.77</i> )	1.24 ( <i>1.13</i> )	1.64 ( <i>1.60</i> )
<b>FIRE 50%</b>	1.35 ( <i>0.98</i> )	1.58 ( <i>1.33</i> )	1.81 ( <i>1.61</i> )	2.18 ( <i>2.00</i> )	2.77 ( <i>2.60</i> )
<b>FIRE 85%</b>	2.73 ( <i>2.59</i> )	2.90 ( <i>2.73</i> )	3.11 ( <i>2.91</i> )	3.35 ( <i>3.15</i> )	3.70 ( <i>3.67</i> )
<b>FIRE 90%</b>	3.14 ( <i>2.90</i> )	3.29 ( <i>3.13</i> )	3.44 ( <i>3.32</i> )	3.66 ( <i>3.57</i> )	4.09 ( <i>4.26</i> )
<b>FIRE 95%</b>	4.19 ( <i>4.25</i> )	4.38 ( <i>4.48</i> )	4.70 ( <i>5.08</i> )	5.56 ( <i>5.56</i> )	5.65 ( <i>6.02</i> )
<b>FIRE MEAN</b>	1.68 ( <i>1.49</i> )	1.92 ( <i>1.76</i> )	2.19 ( <i>2.04</i> )	2.53 ( <i>2.38</i> )	2.91 ( <i>3.03</i> )
<b>FIRE STD</b>	1.58 ( <i>1.55</i> )	1.54 ( <i>1.51</i> )	1.52 ( <i>1.50</i> )	1.54 ( <i>1.51</i> )	1.57 ( <i>1.52</i> )
<b>NO-FIRE 5%</b>	0.16	0.33	0.48	0.60	0.70
<b>NO-FIRE 10%</b>	0.19	0.38	0.55	0.68	0.87
<b>NO-FIRE 15%</b>	0.21	0.42	0.59	0.77	1.12
<b>NO-FIRE 50%</b>	0.31	0.57	0.83	1.25	1.76
<b>NO-FIRE 85%</b>	1.16	1.64	2.01	2.36	2.85
<b>NO-FIRE 90%</b>	1.65	1.98	2.27	2.60	3.05
<b>NO-FIRE 95%</b>	2.22	2.45	2.73	2.99	3.41
<b>NO-FIRE MEAN</b>	0.97	0.98	1.00	1.02	1.08
<b>NO-FIRE STD</b>	0.65	0.93	1.21	1.53	1.98

686

687 **Table 2:** Summary of measured (CALIPSO) smoke plume heights over the entire fire season from  
 688 September 3<sup>rd</sup> to November 9<sup>th</sup> 2006, for days that are statistical outliers. The values here correspond to  
 689 having a mean value more than 85% of less than 15% **in bold**, or a mean value from 80% to 85% or from  
 690 15% to 20% in regular text. The levels are given as a percentile of extinction height over the subset of the  
 691 Maritime Continent impacted by smoke (fire-constrained), based on the MISR observations (**Figure 1**).

	bottom (90% Extinction) [km]	middle-lower (70% Extinction) [km]	median (50% Extinction) [km]	middle-upper (30% Extinction) [km]	top (10% Extinction) [km]
<b>October 11<sup>th</sup></b>	2.29	2.54	<b>3.26</b>	<b>4.11</b>	<b>4.93</b>
<b>October 15<sup>th</sup></b>	1.85	2.20			
<b>October 22<sup>nd</sup></b>	<b>2.55</b>	<b>2.85</b>	2.95		

692

693 **Table 3:** Statistics of measured fire properties (FRP and  $T_F$ ), for all measured fires (**ALL**) and level 9  
694 confidence fires (**L9**) and MERRA meteorological properties ( $T_A$ ,  $v$ ,  $U$ ,  $dT/dz$ ) corresponding to the  
695 geographic locations of **L9**. All data is constrained by the boundaries of the fire extent, and is applicable to  
696 results from the Maximum of the fire season corresponding to October 2006 (**Figure 1**). The distribution's  
697 percentile is given as "**XX%**", the mean and standard deviation are given as "**MEAN**" and "**STD**". Note  
698 that there were no observed fires of L9 on the following dates: 17<sup>th</sup>, 22<sup>nd</sup>, 23<sup>rd</sup>, 24<sup>th</sup>, 25<sup>th</sup>, 26<sup>th</sup>, 27<sup>th</sup>, 29<sup>th</sup>, 31<sup>st</sup>.

	FRP ALL [W/m <sup>2</sup> ]	FRP L9 [W/m <sup>2</sup> ]	$T_F$ ALL [K]	$T_F$ L9 [K]	$T_A$ L9 [K]	V L9 [mm/s]	U L9 [m/s]	$dT/dz$ L9 [K/km]
<b>5%</b>	95.	140.	370.	410.	296.0	0.2	4.1	-5.25
<b>10%</b>	115.	185.	390.	445.	296.4	0.4	4.4	-5.27
<b>15%</b>	130.	230.	400.	480.	296.6	0.6	4.5	-5.28
<b>50%</b>	300.	540.	535.	725.	298.4	1.5	6.0	-5.43
<b>85%</b>	775.	1240.	910.	1275.	301.1	4.1	7.4	-5.65
<b>90%</b>	975.	1495.	1070.	1525.	301.5	4.6	7.7	-5.69
<b>95%</b>	1290.	1855.	1335.	1850.	302.1	5.6	8.1	-5.75
<b>Mean</b>	510.	920.	702.	1029.	298.7	2.1	6.0	-5.44
<b>StD</b>	720.	1340.	573.	1057.	2.0	1.6	1.3	0.16

699

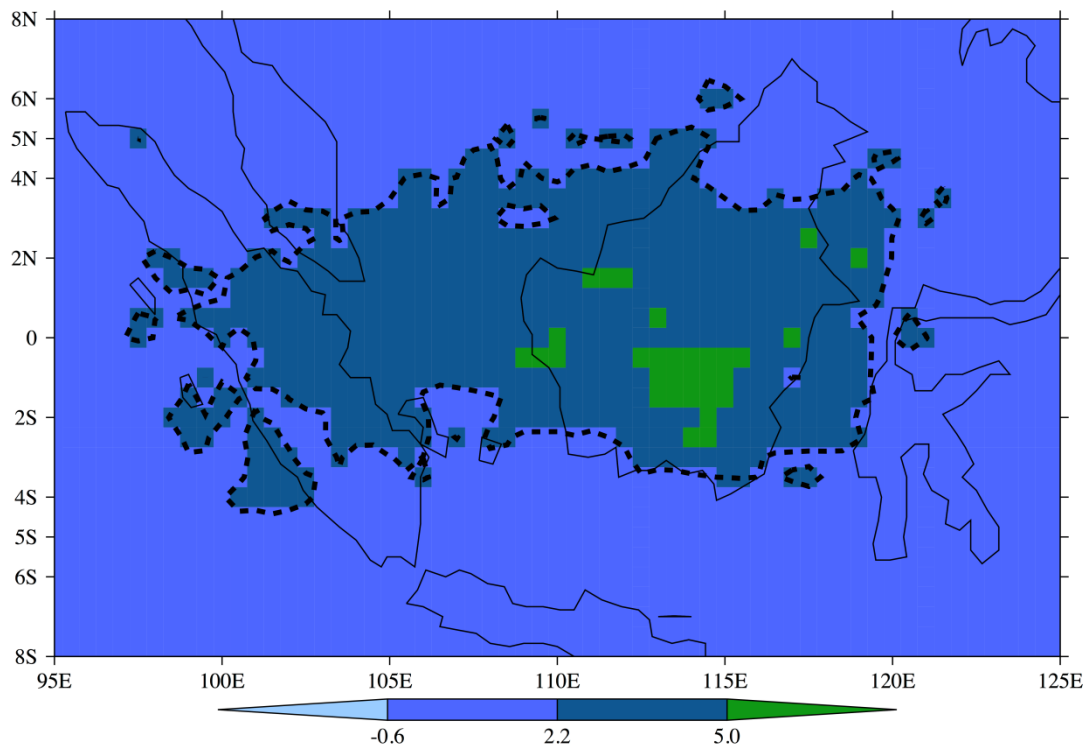


700 **Table 4:** Statistics of the modeled fire heights corresponding to the maximum fire season of October and  
701 the (*Entire fire season*). All values are computed using level 9 confidence fires (**L9**) and MERRA  
702 meteorology ( $T_A$ ,  $v$ ,  $U$ ,  $dT/dz$ ) at the corresponding geographic locations, with the daily average boundary  
703 layer assumed to be 1000m. Sensitivity tests are shown with their respective weighting factor (**1.2, 1.4, 1.6,**  
704 **1.8, or 2.0**) applied to the measured FRP. The modeled heights are given by percentile from the bottom  
705 (5%) to the top (95%), while the mean and standard deviation are given as “**MEAN**” and “**STD**”. Note that  
706 the model was not run on the following days, during which there were no observed **L9** fires: September  
707 13<sup>th</sup>, 14<sup>th</sup>, 15<sup>th</sup>, 16<sup>th</sup>, 17<sup>th</sup>, 27<sup>th</sup>, October 17<sup>th</sup>, 22<sup>nd</sup>, 23<sup>rd</sup>, 24<sup>th</sup>, 26<sup>th</sup>, 27<sup>th</sup>, and 31<sup>st</sup>, and November 2<sup>nd</sup>, 9<sup>th</sup>, 14<sup>th</sup>, 16<sup>th</sup>  
708 through 28<sup>th</sup>, 30<sup>th</sup>.

	<b>FRP(x1.0)</b> [km]	<b>FRP(x1.2)</b> [km]	<b>FRP(x1.4)</b> [km]	<b>FRP(x1.6)</b> [km]	<b>FRP(x1.8)</b> [km]	<b>FRP(x2)</b> [km]
<b>5%</b>	<b>0.41</b> (0.26)	0.44 (0.30)	0.48 (0.33)	0.53 (0.35)	0.56 (0.38)	0.60 (0.41)
<b>10%</b>	<b>0.60</b> (0.41)	0.67 (0.45)	0.73 (0.49)	0.80 (0.53)	0.85 (0.57)	0.91 (0.61)
<b>15%</b>	<b>0.75</b> (0.55)	0.83 (0.61)	0.91 (0.66)	0.98 (0.72)	1.05 (0.77)	1.12 (0.82)
<b>30%</b>	<b>1.14</b> (0.88)	1.28 (0.98)	1.40 (1.07)	1.52 (1.16)	1.63 (1.25)	1.74 (1.33)
<b>50%</b>	<b>1.85</b> (1.40)	2.07 (1.58)	2.27 (1.73)	2.47 (1.88)	2.65 (2.02)	2.82 (2.15)
<b>70%</b>	<b>2.87</b> (2.25)	3.23 (2.52)	3.54 (2.76)	3.84 (3.01)	4.12 (3.23)	4.38 (3.43)
<b>85%</b>	<b>4.21</b> (3.29)	4.66 (3.67)	5.11 (4.02)	5.53 (4.35)	5.87 (4.64)	6.22 (4.92)
<b>90%</b>	<b>4.99</b> (3.95)	5.54 (4.40)	6.08 (4.80)	6.58 (5.21)	6.97 (5.56)	7.41 (5.87)
<b>95%</b>	<b>6.10</b> (5.25)	6.79 (5.86)	7.43 (6.39)	7.76 (6.83)	8.16 (7.22)	8.61 (7.57)
<b>Mean</b>	<b>2.41</b> (1.94)	2.69 (2.17)	2.96 (2.38)	3.21 (2.58)	3.44 (2.77)	3.67 (2.95)
<b>StD</b>	<b>1.98</b> (1.76)	2.21 (1.96)	2.42 (2.15)	2.62 (2.33)	2.81 (2.50)	2.99 (2.65)

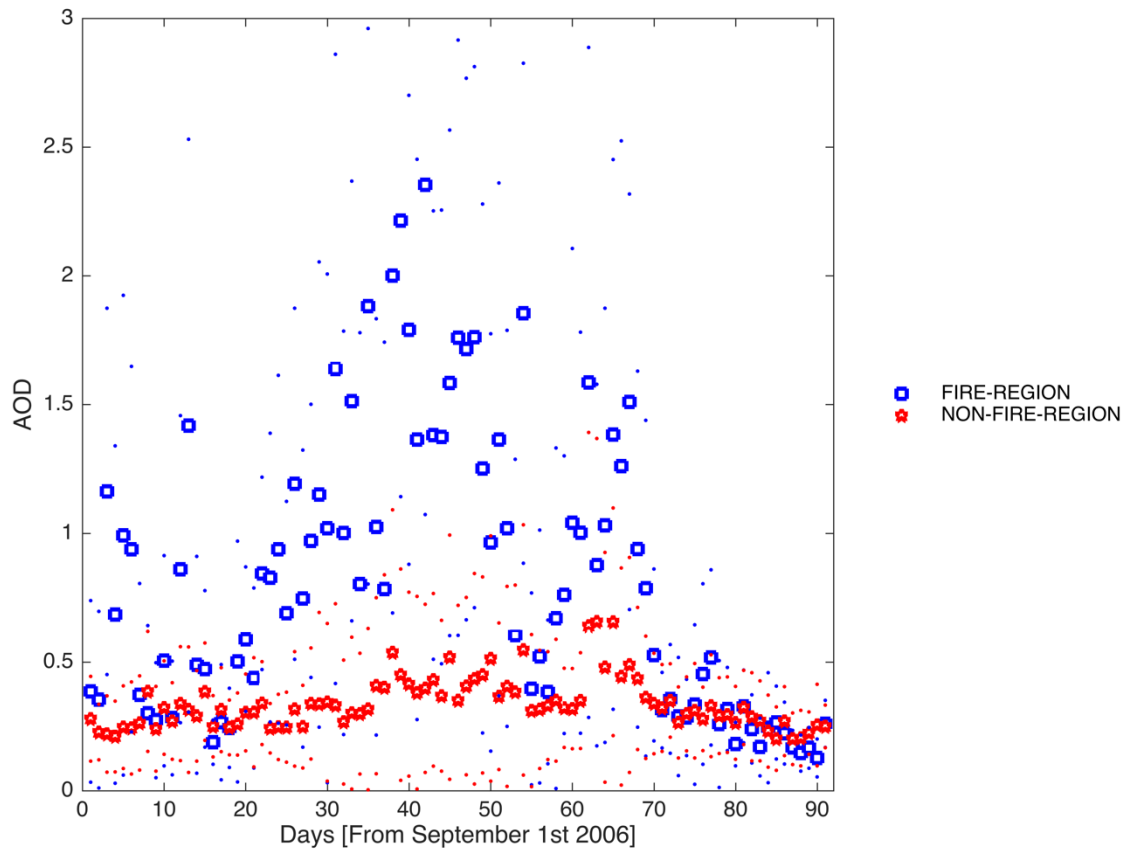
709

710 **Figure 1:** Map of Maritime Continent. The smoke plume impacts the sub-region contained within the  
711 dashed lines, or the so-called **fire-constrained** region. On the other hand, the region outside of the dashed  
712 lines is the so-called **non fire-constrained** region. The colors on the plot correspond to the intensity of the  
713 variance, as explained in Cohen [2014]. The plot is based on a variance maximization technique applied to  
714 the measurements from all MISR overpasses from 2000 through 2014 (Cohen, 2014). Note that in this part  
715 of the world 1 degree of latitude or longitude is approximately 100km, leading to a fire-impacted region  
716 over 2500km across.



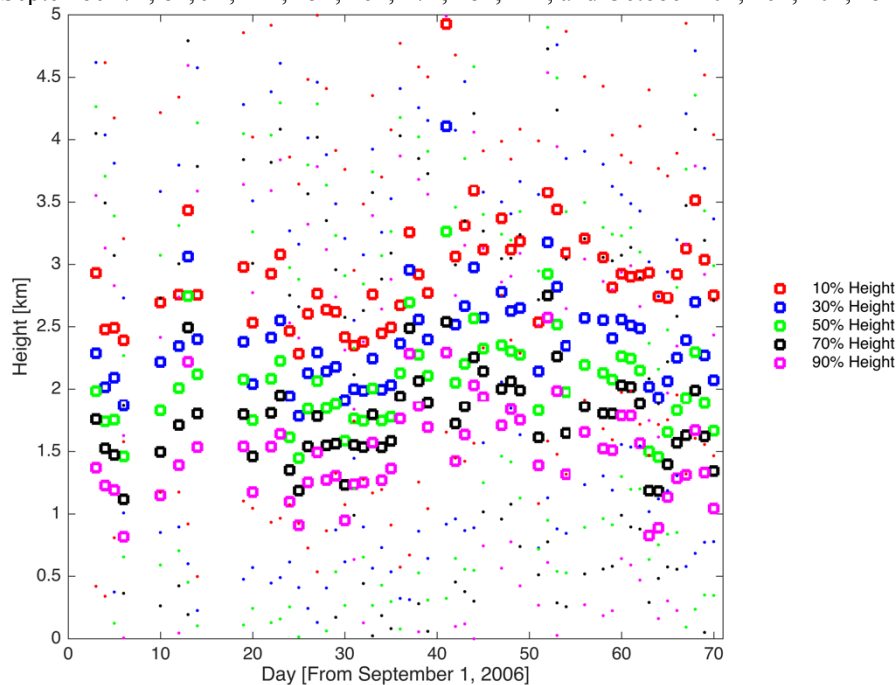
717

718 **Figure 2:** Time series of daily averaged measured AOD over the fire-constrained regions of the Maritime  
719 Continent [blue], and the non fire-constrained regions of the Maritime Continent [red], as given in **Figure**  
720 **1.** Circles are computed daily mean values, while dots are computed daily standard deviation bands. Note  
721 that this figure contains the daily data from September 1, 2006 through November 30<sup>th</sup>, 2006.



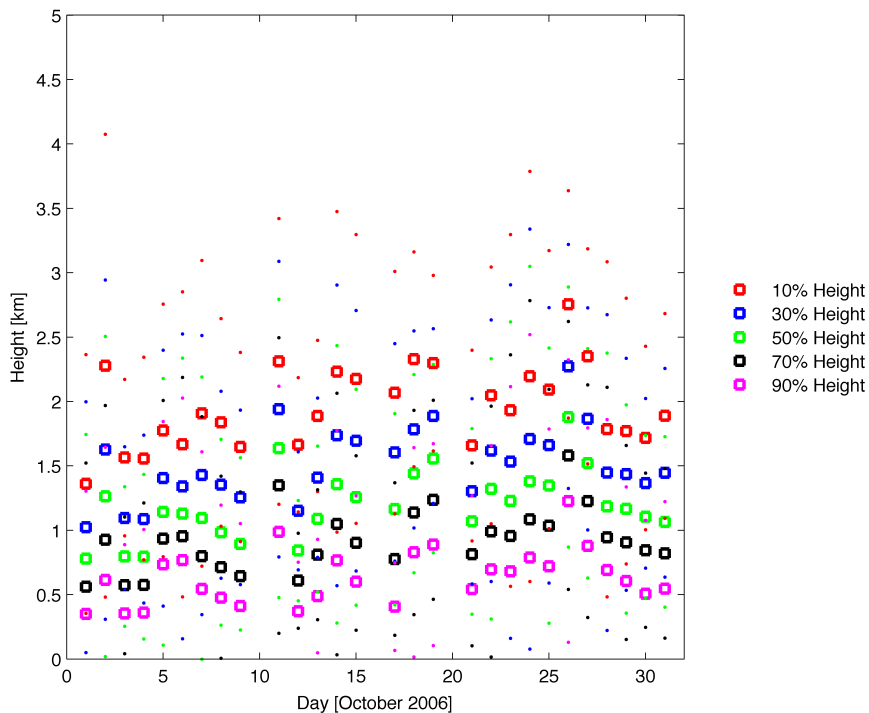
722

723 **Figure 3a,3b:** Time series of measured CALIPSO extinction heights over the fire constrained (A) and non  
 724 fire-constrained (B) regions as given **Figure 1**. Note that for the fire constrained region, the analysis (and  
 725 hence the data) has been extended for the period from September 3<sup>rd</sup> through November 9<sup>th</sup>. For both plots,  
 726 the dots correspond to the height of the column integrated backscatter at: 10% [red] (top), 30% [dark blue],  
 727 50% [yellow], 70% [black], and 90% [light blue] (bottom). The circles are computed daily means, while  
 728 dots are the computed daily standard deviation bands. There was no measurement over the region on  
 729 September 7<sup>th</sup>, 8<sup>th</sup>, 9<sup>th</sup>, 11<sup>th</sup>, 15<sup>th</sup>, 16<sup>th</sup>, 17<sup>th</sup>, 18<sup>th</sup>, 21<sup>st</sup>, and October 10<sup>th</sup>, 16<sup>th</sup>, 20<sup>th</sup>, 25<sup>th</sup>, and 27<sup>th</sup>.



730  
731

(A)



732

(B)

733 **Figure 4:** Time series of measured extinction height levels for the median heights (red circles and line) with  
 734 their corresponding +1 standard deviation range (red dotted line), and respective middle-upper (blue), and  
 735 middle-lower (yellow), are given below. The best fitting modeled heights for the median daily boundary  
 736 layer height of 1000m are given as black x's, and are found to be respective FRP enhancements of 1.0, 1.2,  
 737 and 1.4. The best fitting modeled heights for the low daily boundary layer height of 700m are given as  
 738 black +'s, and are found to be respective FRP enhancements of 1.0, 1.1, and 1.2. The best fitting modeled  
 739 heights for the high daily boundary layer height of 1300m are given as black o's, and are found to be  
 740 respective FRP enhancements of 1.0, 1.4, and 1.8.

